Journal of Materials Chemistry A

Accepted Manuscript

This article can be cited before page numbers have been issued, to do this please use: N. Nelson, Z. Wang, P. Naik, J. S. Manzano, M. Pruski and I. I. Slowing, *J. Mater. Chem. A*, 2017, DOI: 10.1039/C6TA08703E.

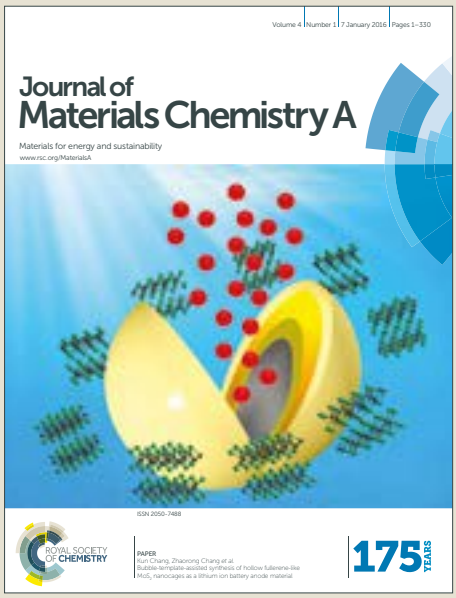

ROYAL SOCIETY OF CHEMISTRY

rsc.li/materials-a

View Article Online
DOI: 10.1039/C6TA08703E

Journal Name

ARTICLE

Phosphate modified ceria as a Brønsted acidic/redox multifunctional catalyst

Received 00th January 20xx,
Accepted 00th January 20xx

DOI: 10.1039/x0xx00000x

www.rsc.org/

Nicholas C. Nelson,[a,b] Zhuoran Wang,[a,b] Pranjali Naik,[a,b] J. Sebastián Manzano,[a,b] Marek Pruski[a,b] and Igor I. Slowing*[a,b]

Deposition of trimethylphosphate onto ceria followed by thermal treatment resulted in formation of surface phosphates with retention of ceria fluorite structure. The structural and chemical properties of phosphate-functionalized ceria were studied using ^{31}P solid-state NMR, XPS, zeta titration, ammonia thermal desorption, pyridine adsorption, and model reactions. The introduction of phosphates generated Brønsted acidic sites and decreased the number of Lewis acidic sites on the surface. The relative amount of Lewis and Brønsted acids can be controlled by the amount of trimethylphosphate used in the synthesis. Upon deposition of Pd, the multifunctional material showed enhanced activity for the hydrogenolysis of eugenol compared to Pd on the unmodified ceria support. This was attributed to the cooperativity between the Lewis acid sites, which activate eugenol for dearomatization, and the redox/Brønsted acid property, which catalyzes hydrogenolysis.

Introduction

Ceria (CeO_2) is a unique material in catalysis science due to its inherent redox properties.[1, 2] Many ceria-based technological applications rely on the facile Ce^{3+}/Ce^{4+} redox cycle, which supplies reactive oxygen species to substrates.[3] Perhaps the most notable is three-way catalysis, but other uses (reforming processes, water-gas shift reaction, solid oxide fuel cells, etc.) are emerging and are expected to be industrialized soon.[4] Fundamental research and continued atomistic understanding of the structure and formation of ceria redox-active sites has led to the development of complex ceria-based materials with enhanced redox capability.[5-14] In the past decade, synthetic procedures have been developed that allow strict geometric control over ceria particle morphology resulting in materials that selectively expose specific sets of lattice planes.[15-18] These materials and their enhanced defect-mediated redox capabilities have led to the development of ceria-based catalytic systems for organic transformations, especially as they relate to redox processes.[19-22]

In contrast to the extensive progress made towards understanding and engineering redox sites in ceria-based materials, limited efforts have been devoted to incorporate additional functionalities to their surface.[23] Yet, developing methods to add surface functionalities while retaining redox activity could provide multipurpose materials capable of performing specialized tasks and tandem processes. Furthermore, incorporation of surface functionalities may offer precise control over activity and selectivity in catalytic conversions.[23, 24] One simple, yet important functionality that can be added to ceria is Brønsted acidity. Ceria exhibits weak Lewis acidity and its surface hydroxyl groups show little to no Brønsted acid character.[25-28] Brønsted acidic sites have been introduced through impregnation of ceria with tungsten and vanadium precursors followed by calcination to yield supported oxides.[29-32] Ceria-supported tungsten oxides and their analogs are perhaps the most widely known ceria-based materials exhibiting Brønsted acidity due to their activity in the selective catalytic reduction of NO_x with NH_3.[33-35] Another class of ceria-based materials with Brønsted acidity was developed through sulfonation of ceria-zirconia mixed metal oxide.[36-38]

An attractive alternative option for introducing Brønsted acidity to the surface is through organophosphate precursors. Organophosphates represent a versatile class of compounds that can be specifically tailored with desired organic functional groups for target applications.[39-41] Immobilization of organophosphates with varying organic components on ceria may allow material properties to be tuned[42] and enable cooperativity with the intrinsically active sites of the supporting material to control catalytic activity and/or product selectivity.[43-45] For example, hydrogenolysis reactions relevant to biomass processing can be catalyzed by acid and redox-active sites.[46-51] Under typical reaction conditions, oxygen substituents can be activated towards C-O bond cleavage through protonation by the acid component or binding to oxophilic vacancies in the redox-active component. Therefore, the introduction of acidic sites to a redox-active material could lead to a higher hydrogenolysis activity. In this context, this

[a] US DOE Ames Laboratory, Ames, Iowa 50011, United States
[b] Department of Chemistry, Iowa State University, Ames, Iowa 50011, United States

Electronic Supplementary Information (ESI) available: additional P-content measurements, DRIFT, XPS, SSNMR spectra, TPD profiles, XRD patterns, and catalytic reaction data. See DOI: 10.1039/x0xx00000x

work explores the structure and catalytic properties of phosphate-functionalized ceria.

Previous studies have indicated that the thermal decomposition of organophosphates and closely related organophosphonates on metal oxides produces surface-adsorbed alkoxides and surface-bound phosphates.[52-58] It is thought that the first step occurs via coordination of the phosphoryl oxygen with a metal cation. Cleavage of an alkoxide follows shortly thereafter, and can occur at low temperature. Upon subsequent heating, the methoxy groups undergo disproportionation to yield methanol, formaldehyde, and surface-bound phosphates. Thus, it would be expected that P-OH bonds could be formed through hydrolysis during air calcination and give rise to acid functionality. Prior studies also showed that high temperature (600 °C) treatment of P-containing compounds deposited onto ceria can lead to formation of subsurface $CePO_4$ (monazite) crystals without Brønsted acid functionality.[59-61] Monazite formation implies reduction of cerium(IV) to cerium(III), with the extent of reduction depending on phosphorus loading.[60, 61] This leads to the undesirable inhibition of redox properties. A potential approach to prevent overreduction and monazite formation may be through the use of high-surface area ceria and lower calcination temperatures. For a fixed phosphorus loading, high-surface-area ceria should accommodate higher amounts of surface phosphates due to the higher amount of surface Ce-atoms that coordinate to the phosphoryl group; low-surface-area supports would contain fewer surface phosphates, with the excess penetrating into the bulk. Similarly, lower calcination temperatures would prevent sintering that likely contributes to bulk phosphate formation. In this study, deposition of trimethylphosphate onto high-surface-area ceria, followed by low-temperature calcination, led to a bifunctional (redox and acid) material (Scheme 1). Upon deposition of palladium, the multifunctional material showed higher eugenol hydrogenolysis activity than palladium on unmodified ceria.

Scheme 1. Proposed bifunctional redox/acid material.

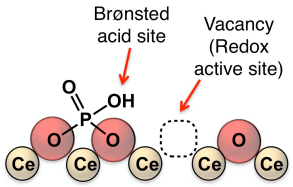

Experimental

Reagents

Cerium(III) nitrate hexahydrate, trimethylphosphate, propylene oxide, deuterium oxide, 1,4-dioxane, indigo carmine, and pyridine were purchased from Sigma Aldrich. Potassium nitrate, sodium hydroxide, ammonium acetate, nitric acid, hydrogen peroxide, acetic acid, and hydrochloric acid were purchased from Fisher. Pluronic P104 was obtained from BASF. Cerium(III) nitrate hexahydrate was dried under vacuum at room temperature for 48 h prior to all synthetic methods. All other chemicals were used without further purification. All reagents met or exceeded ACS specifications.

Synthesis of ceria (CeO_2)

The method was adopted from a previously published report.[62] Briefly, $Ce(NO_3)_3 \bullet 6H_2O$ (8.8 g, 20.3 mmol) and Pluronic P104 (10.1 g) were dissolved in ethanol (200 mL). The contents were stirred vigorously until complete dissolution (~2 h). The solution was cast into a large crystallization dish and placed in a pre-heated 65 °C oven until the ethanol had evaporated (~8 h). The resulting gel was placed in a pre-heated 150 °C oven overnight. The yellow powder was subsequently calcined in air at 450 °C for 4 h with a ramp rate of 2 °C min^{-1}. Caution! During thermal treatment at 150 °C, combustion occurs within ~12 min, producing flames which self-extinguish within seconds after all combustible material (i.e., block copolymer) is burned. The thermal treatment step should be conducted in an oven, preferably in a fume hood with a closed sash to avoid exposure to gaseous decomposition products.

Synthesis of phosphate-modified ceria (CeO_2-PO_x)

The synthesis of phosphate-modified ceria was accomplished through an impregnation route. In a typical procedure, the desired amount of trimethylphosphate (TMP) was deposited onto the CeO_2 support in five increments. That is, five cycles of TMP impregnation, followed by thorough mixing with a mortar and pestle, were performed until the total desired amount of TMP was added to the CeO_2 support. The material was calcined at 450 °C for 4 h with a 10 °C min^{-1} ramp rate.

Synthesis of Pd/CeO_2 and Pd/CeO_2-PO_x

In a typical procedure, palladium (II) acetate (1 wt. % Pd) was dissolved in acetone and impregnated onto the support. The precatalysts were heated in air to 350 °C at 2.5 °C min^{-1} and held for 2 h. After cooling to room temperature, the catalysts were heated under flowing H2 (50 mL min^{-1}) using the same temperature program.

Powder X-ray diffraction (PXRD)

Diffraction patterns were collected using Co Kα1, Kα2 split radiation (45 kV, 40 mA, λavg = 1.7903 Å) on a PANalytical X'Pert PRO diffractometer equipped with a theta–theta vertical mode goniometer, incident Fe filter, an air-cooled X'Celerator real time multiple strip (RTMS) detector, and spinner stage. Patterns were converted to Cu Kα radiation for comparison to standards using Bragg's law. Samples were prepared by placing powders onto a background-less holder. Crystallite sizes were calculated using Scherrer equation.

Surface area and porosimetry

Textural properties of the supports and catalysts were measured by nitrogen sorption isotherms at -196 °C in a

Micromeritics Tristar analyzer. The surface areas were calculated by the Brunauer-Emmett-Teller (BET) method. Sample pretreatment for surface area measurement was done by flowing N_2 for 6 h at 100 °C.

Inductively coupled plasma-optical emission spectroscopy (ICP-OES)

Ce, P, and Pd loadings were analyzed by a Perkin Elmer Optima 2100 DV Inductively Coupled Plasma-Optical Emission Spectroscope (ICP-OES). Samples (ca. 10 mg) were digested in 5 mL of 4 M HCl, 1 mL of concentrated HNO_3, and 2 mL of 30 v/v % H_2O_2. The samples were sonicated for ten minutes. Then they were placed into a 50 °C water bath for ~12 h. Each sample was then diluted to 10 mL of total solution.

Diffuse reflectance infrared fourier transform spectroscopy (DRIFTS)

Measurements were made on a Bruker Vertex 80 FT-IR spectrometer with OPUS software and apodized spectral resolution of 0.2 cm^{-1}. The spectrometer was equipped with a HeNe laser and photovoltaic MCT detector. A Praying Mantis™ diffuse reflectance accessory and high temperature reaction chamber were used for room and variable temperature measurements, respectively. 32 scans were collected for each measurement in absorbance mode with 8 cm^{-1} resolution. For pyridine adsorption experiments, the samples were heated to 100 °C in He flow (50 mL min^{-1}) for 60 minutes and the samples were subsequently cooled to room temperature under He flow. Blank spectra were recorded at this time. Then, the He flow was redirected through a saturator containing pyridine at room temperature. Spectra were taken at 1 min intervals under probe molecule exposure until the formation of liquid-like bands was observed (~1-5 min). At this time, the He flow was redirected away from the saturator. Spectra were taken at 10 min intervals until no changes were observed between subsequent spectra (~20-30 min).

X-ray photoelectron spectroscopy (XPS)

XPS analysis was done with a PHI 5500 multitechnique system using a standard Al X-ray source. Samples were analyzed at room temperature with no special preparation. Charge correction was accomplished by shifting the Ce 3d v-peak to 882.6 eV for all spectra.[63, 64] All spectra were normalized so that the most intense peak had a value of 1.

Solid state nuclear magnetic resonance (SSNMR)

The SSNMR measurements were performed on a 400 MHz (9.4 T) Agilent DD2 spectrometer equipped with a 3.2-mm Chemagnetics double resonance magic angle spinning (MAS) probe, and on a 600 MHz (14.1 T) Varian DD1 spectrometer equipped with a 1.6-mm FastMAS™ T3-type probe. Samples were directly packed into zirconia rotors without any further treatment. The ^1H background-free MAS spectra of all samples were obtained by subtracting the signal measured with an empty probe. The ^1H Hahn echo spectra were obtained using pulse sequence (90° - τ - 180° - τ) with various echo delays synchronized with MAS period. The 1D ^{31}P spectra were obtained under MAS using direct polarization (DPMAS) and a $^{31}P\{^1H\}$ tangent-ramped cross polarization scheme (CPMAS). The same CP scheme was used to generate the 2D $^{31}P\{^1H\}$ heteronuclear correlation (Hetcor) spectra. The double-quantum/single-quantum (DQ/SQ) experiments were performed using the back-to-back (BABA) pulse sequence.[65] The ^1H chemical shifts are reported relative to tetramethylsilane (TMS), and the ^{31}P chemical shifts are reported relative to phosphoric acid (H_3PO_4, 85% in D_2O). The detailed parameters are given in the corresponding figure captions using the following symbols: ν_R denotes the MAS rate; $\nu_{RF}(X)$, the magnitude of the RF field applied to X nuclei; τ_{CP}, the cross-polarization contact time; τ_{rd}, the recycle delay and $\Delta\tau_1$, the increment of τ_1 in 2D experiments.

Scanning Transmission Electron Microscopy (STEM)

Materials imaging and elemental mapping was carried out on a FEI Titan Themis Cubed aberration corrected scanning transmission electron microscope (STEM) operating at 200kV (Cs corrector point-to-point resolution <0.06 nm). Samples were prepared by placing 2-3 drops of dilute ethanol suspensions onto lacey-carbon-coated copper grids. Elemental mapping was performed using energy dispersive X-ray spectroscopy (EDS).

Temperature programmed desorption (TPD)

NH_3-TPD experiments were carried out using a Micromeritics AutoChem II equipped with TCD detector. The samples (ca. 300 mg) were placed into a quartz U-tube and degassed at 500 °C for 60 minutes (10 °C min^{-1}) under O_2-He (10 % O2) flow (50 mL min^{-1}). The samples were cooled to 100 °C under O_2-He and the gas flow switched to NH_3-He (10 % NH_3). After 15 minute exposure, the gas flow was switched to He and held at 100 °C for 15 minutes before cooling to 40 °C. The temperature was then ramped at 10 °C min^{-1} while monitoring the TCD signal.

Zeta potential measurements

Zeta potential measurements were made on a Zetasizer Nano ZS90 instrument with a standard 633 nm He-Ne laser using the Smoluchowski approximation. Samples were prepared by suspending the solid (~10 mg) in aqueous KNO3 (0.01M, 10 mL). The pH of the suspension was adjusted with dilute NaOH and HCl solutions. Afterwards, the samples were sonicated for 30 minutes and then allowed to sit for varying amounts of time in order to obtain reliable data.

Cationic exchange

Two samples with different masses (ca. 10 and 100 mg) for each material were weighed into 20 mL scintillation vials. The solids were suspended in aqueous ammonium acetate (0.1 M, 10.0 mL, pH = 6.99). After 24h, with periodic agitation, the pH of the suspension was measured. The measured pH was related to the exchangeable H^+ on the materials through a

calibration curve. The calibration curve was constructed by adding a known amount of standardized acetic acid solution (0.0984 ± 0.003 M) to ammonium acetate solution (0.1 M, 10.0 mL, pH = 6.99) and measuring the pH after each addition (20-40 µL). The curve was fit to a third order polynomial with a correlation coefficient of 0.9991 in the pH range of 6.99-6.01.

Deuterolysis of propylene oxide

In a typical reaction, ~10 mg of catalyst, 1 mL of D_2O, and a stir bar were placed into 4 mL glass vial. The vial was then placed into an OptiBlock parallel synthesis reaction block (OP500 series) equipped with thermocouple, locking base, locking plate, and PTFE faced silicone septa pad. Once the vials were sealed, propylene oxide (40 µL, 0.6 mmol) was added via syringe. The reactor assembly was heated to the desired temperature for the desired time with stirring (200 rpm). Afterwards, the reactor assembly was allowed to cool to room temperature, at which time the catalyst was separated by centrifugation. The supernatant (1 mL) was analyzed by ^{1}H-NMR using 1,4-dioxane (5 µL, 58 µmol) as internal standard. The ^{1}H-NMR spectra were collected on a Bruker DRX 500 equipped with a narrow bore 11.7T/500 MHz magnet and a standard ^{1}H probe. ^{1}H-NMR (deuterium oxide, 500 MHz, 25 °C): δ, ppm: 1.07 (3H, s, CH3); 3.37 (1H, dd, CHa); 3.47 (1H, dd, CHb); 3.81 (1H, sext, CH). Mass balances were 94-100 %.

Photodegradation of indigo carmine

A 2.0 mL aliquot of an aqueous indigo carmine stock solution (18.3 mg L^{-1}) was added to 4.1 mg of catalyst in a 4 mL glass vial. The suspension was allowed to pre-equilibrate in the dark for 0.5 h. Afterward the vials were placed into a Rayonet RPR-200 photoreactor with a 350 nm light source under stirring for 1.5 h. The photodegradation activity was monitored by comparing the absorbance of indigo carmine solution before and after the reaction using a UV/VIS spectrometer.

Eugenol and guaiacol hydrotreatment

Hydrogenation reactions were carried out using a high pressure reactor. The Pd/CeO_2-yPO_x catalysts (ca. 50 mg) were placed into the reactor along with water (25 mL) and substrate (97 µmol). The reactor was purged with nitrogen and then pressurized with H_2 (10 bar). The contents were heated to 100 °C (10 °C min^{-1}) and held for 4 h under mechanical stirring (800 rpm). The reactor was allowed to cool to room temperature (~0.5 h). The products were extracted with ethyl acetate (25 mL) and analyzed by GCMS (7890A, 5975C with HP-5MS column). Mass balances were between 90 and 100 %.

Results and discussion

Phosphate-functionalized ceria (CeO_2-PO_x) was prepared by impregnation of CeO_2 with trimethylphosphate (TMP) followed by calcination at 450 °C for 4 h. The maximum loading of P-containing compounds on the CeO_2 support was about 0.23 moles of P per mole of Ce (i.e. P:Ce = 0.23) (Fig. S1). This loading corresponds to about 7.4 P-atoms nm^{-2} and essentially represents surface saturation as the theoretical amount of Ce atoms on the (111) surface is about 7.9 Ce-atoms nm^{-2}.[66] The physical and chemical properties of two samples with nominal P:Ce loadings of 0.1 and 0.2, denoted as CeO_2-0.1PO_x and CeO_2-0.2PO_x, are listed in Table 1. The specific surface areas of the P-containing materials were lower than the unmodified CeO_2 support. Control experiments indicated the decrease was not due to additional calcination time but related phosphate formation. The PXRD pattern for all materials could be indexed to the fluorite structure of ceria with no other reflections observed (Fig. 1). This indicates that crystalline phosphate phases were not formed as in previous reports with similar P:Ce loadings.[60, 61] The difference can be attributed to the significantly lower surface area (13 m^2 g^{-1}) and higher calcination temperature (600 °C) used in the previous studies. Here, the PXRD analysis showed the CeO_2 crystallite sizes and lattice parameters increased only slightly upon phosphorus modification (Table 1). The elongation of the ceria lattice has previously been attributed to higher concentrations of Ce(III) due to phosphate binding (i.e. $CePO_4$).[60, 61] STEM mapping showed P-species were well dispersed onto the CeO_2 support (Fig. S2) with no obvious change in support morphology.[62] The presence of surface phosphates was further confirmed through DRIFTS analysis as indicated by the appearance of bands between 1200-900 cm^{-1}, which are characteristic for the ν(P-O) of phosphates (Fig. S3a).[52-54, 57, 67-69] There was also a band present around 2400 cm^{-1} for the phosphate-containing samples that was not present for CeO_2 (Fig. S3b). This band is consistent with P-OH through comparison with the IR spectrum for monobasic sodium phosphate.[70]

Table 1 Physical properties of the materials.

Sample	P Loading[a]		Surface Area	Crystallite Size	Lattice Parameter
	(mmol g^{-1})[b]	(nm^{-2})	(m^2g^{-1})[c]	(nm)[d]	(Å)[e]
CeO_2	0	0	213	6	5.413
CeO_2-0.1PO_x	0.64±0.05	3.5	110	8	5.417
CeO_2-0.2PO_x	1.1±0.1	5.8	115	9	5.421

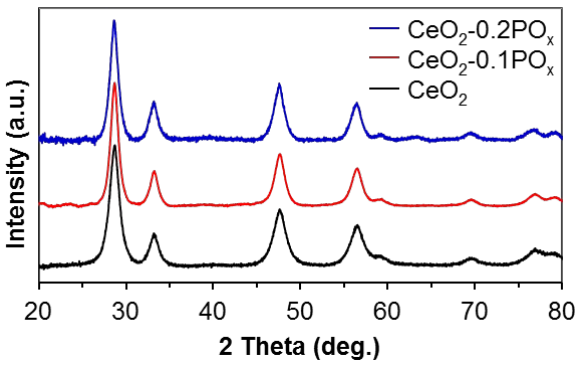

Fig. 1 PXRD patterns of the ceria and phosphate-modified ceria materials.

View Article Online
DOI: 10.1039/C6TA09703F

The electronic structure of the materials was probed via XPS to determine the nature and valency of surface species. The Ce 3d spectral region (Fig. 2) for both P-containing materials and CeO_2 displayed bands consistent with those reported for fully oxidized ceria.[63, 64, 71] A slight increase in intensity was observed around 885 and 904 eV for the P-containing materials, possibly due to the v' and u' bands of Ce(III), respectively.[71-74] This increased Ce(III) band intensity was consistent with the increased lattice parameters for P-containing materials. The O 1s spectrum for all three materials showed a band centered around 529.5 eV (Fig. S4a). Additional intensity for the phosphate-impregnated materials was observed at higher binding energies, suggesting oxygen species different from those observed for CeO_2. The P 2p spectrum for CeO_2-0.1PO_x and CeO_2-0.2PO_x showed one band centered around 133.1 eV, which is also consistent with phosphates (Fig. S4b).

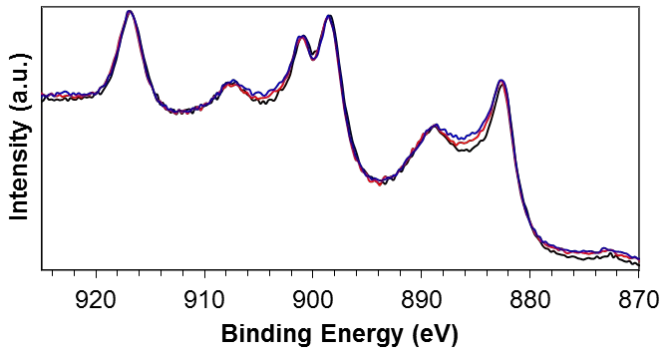

Fig. 2 XPS spectra for CeO_2 and phosphate-functionalized CeO_2 in the Ce 3d spectral region.

The solid-state (SS)NMR ^{31}P spectra of CeO_2-0.1PO_x and CeO_2-0.2PO_x were measured using direct polarization (DP) or $^{31}P\{^1H\}$ cross polarization (CP) under magic angle spinning (MAS), as detailed in the Supporting Information. The experimental parameters are given in the figure captions, where ν_R denotes the MAS rate; $\nu_{RF}(X)$, the magnitude of the RF field applied to X nuclei; τ_{CP}, the CP contact time; τ_{rd}, the recycle delay and $\Delta\tau_1$, the increment of τ_1 in 2D experiments. The ^{31}P DPMAS spectra of both samples contained a strong peak at around -5 ppm with the line width at half height of roughly 10 ppm (Fig. 3), which was flanked by a pair of spinning sidebands, marked with asterisks. Additionally, the spectrum of CeO_2-0.2PO_x featured a less intense and broader peak centered at around 0 ppm. Identical line shapes were observed in the $^{31}P\{^1H\}$ CPMAS spectra (Fig. S5). By comparing the total integrated intensity of DPMAS spectra with that of a reference sample measured under identical conditions ($NH_4H_2PO_4$), the phosphorus loading was estimated at 0.42 (±0.04) mmol g^{-1} for CeO_2-0.1PO_x and 0.73 (±0.07) mmol g^{-1} for CeO_2-0.2PO_x. These estimates were lower, by about one-third, than those obtained by the ICP analysis (Table 1), which may be attributable, at least in part, to paramagnetic broadening. The presence of paramagnetic species in both samples was also suggested by the short T_1 relaxation times of phosphorous, which were about 1 and 2 seconds for these two samples, respectively. However, while these ^{31}P relaxation times were much shorter than those typically encountered in diamagnetic solids,[75] T_1 values on the order of 10 ms were reported in heavily paramagnetic $CePO_4$ nanoparticles.[76] The ratios between the phosphorus loadings in CeO_2-0.1PO_x and CeO_2-0.2PO_x obtained by SSNMR and ICP were almost identical (1 : 1.74 and 1: 1.72, respectively).

To assign the ^{31}P peaks, the 2D $^{31}P\{^1H\}$ heteronuclear correlation (Hetcor) spectra of CeO_2-0.1PO_x and CeO_2-0.2PO_x were measured using the CP scheme for $^1H \rightarrow ^{31}P$ magnetization transfer (Fig. 4). In both samples, the ^{31}P sites were correlated to two types of protons, resonating at 5.2 ppm and ~8.2 ppm. The ^1H peak at 5.2 ppm coincided with the single resonance observed in an unmodified CeO_2 support (Fig. S6), and was thus assigned to water weakly bound to ceria. The ^1H peak at around 8.2 ppm was attributed to P-OH groups of the surface attached phosphates, as it only appeared in phosphate-impregnated materials and its chemical shift fell into the range typical for P-OH species (between 7.0–16.8 ppm).[77] These assignments were further supported by the long T_2` relaxation times associated with both resonances (Fig. S7). Based on these 1D and 2D spectra, the dominant ^{31}P peak can be assigned to orthophosphate- and/or pyrophosphate-type functionalities, including some P-OH species, bound to the CeO_2 support. The orthophosphate species in inorganic phosphates are known to resonate near 0 ppm (typically between -5–10 ppm), whereas pyrophosphates are typically observed only a few ppm upfield from this range.[77, 78] Following the earlier study by Karpowich et al.,[76] the broad ^{31}P peak centered at around 0 ppm in CeO_2-0.2PO_x was attributed to the amorphous phosphate-rich phase.

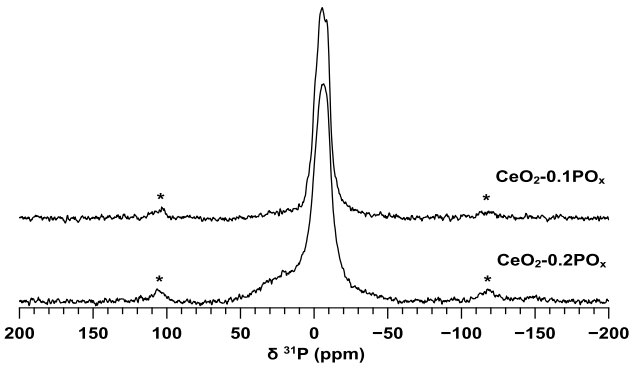

Fig. 3 ^{31}P DPMAS spectra of CeO_2-0.1PO_x and CeO_2-0.2PO_x. The spectra were obtained at 9.4 T using ν_R = 18 kHz, $\nu_{RF}(^{31}P\ 90^\circ)$ = 83.3 kHz, $\nu_{RF}(^1H$ SPINAL-64) = 100 kHz, and 128 scans with τ_{rd} = 10 s for CeO_2-0.1PO_x and τ_{rd} = 6 s for CeO_2-0.2PO_x.

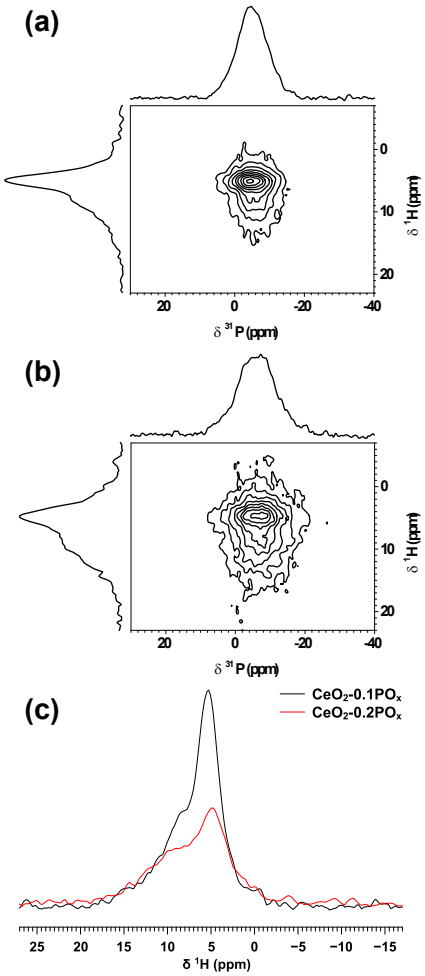

Fig. 4 2D $^{31}P\{^{1}H\}$ Hetcor spectra of (a) CeO_2-0.1PO_x and (b) CeO_2-0.2PO_x. The spectra were obtained at 9.4 T using ν_R = 18 kHz, τ_{CP} = 2.1 ms, $\nu_{RF}(^{1}H\ CP)$ = 96 kHz, $\nu_{RF}(^{31}P\ CP)$ = 78 kHz, $\nu_{RF}(^{1}H\ SPINAL\text{-}64)$ = 96 kHz, Δt_1 = 55 µs, 128 (a) or 256 (b) scans per row, and τ_{rd} = 1 s. (c) Comparison of the ^{1}H projections of CeO_2-0.1PO_x (black line) and CeO_2-0.2PO_x (red line).

To distinguish between the orthophosphate and pyrophosphate species, the homonuclear *through-space* correlations between ^{31}P nuclei were measured by using the double-quantum/single-quantum (DQ/SQ) MAS NMR experiment.[65, 79, 80] Rather than acquiring the entire 2D DQ/SQ dataset, which would have been time consuming and unnecessary given the lack of resolution, the evolution time t_1 was fixed to zero and the intensity of 1D DQ-filtered spectra was measured as a function of the excitation and reconversion times τ_{DQ}. Such τ_{DQ}-dependence, which is often referred to as the build-up curve, can be used to estimate the average ^{31}P-^{31}P distance between the interacting spins. The DQ-filtered spectra of CeO_2-0.1PO_x and CeO_2-0.2PO_x (Fig. S8) exhibited the same line shape as one observed by ^{31}P DPMAS, except for the broad peak at 0 ppm in CeO_2-0.2PO_x, which may have been attenuated due to fast relaxation. As can be seen in Fig. S9a,b, the maximum signal was observed at $\tau_{DQ} \approx 1.0$ ms for CeO_2-0.2PO_x and at $\tau_{DQ} \approx 1.1$ ms for CeO_2-0.1PO_x which, according to simulations performed using SIMPSON program (Fig. S9c,d),[79] corresponds to average ^{31}P-^{31}P distances of ~3.4 Å and 3.5 Å, respectively. These are approximate values, based on a two-spin model, and most likely distributions of distances exist in both samples. However, these values differ significantly from those measured for a reference sample containing pyrophosphate species ($Ca_2P_2O_7$), which exhibited a maximum of the build-up curve at less than 0.5 ms, in approximate agreement with the ^{31}P-^{31}P distance of ~2.9 Å. An attempt to achieve a *through-bond* (^{31}P-O-^{31}P) polarization transfer in CeO_2-0.2PO_x using the INADEQUATE experiment,[80] did not result in any measurable signal. While the DQ/SQ experiments and INADEQUATE are not sufficiently sensitive to unequivocally exclude the presence of any pyrophosphate species in these samples, they strongly suggest that closely spaced orthophosphates were the dominant surface species in both samples.

The SSNMR measurements indicated hydroxyl groups were attached to phosphorus, which should affect the acid-base properties. Thus, zeta potential titrations were used to evaluate the acid-base properties of the material. The zeta potential represents the average potential difference between the diffuse layer (i.e. surface of shear or shear plane) of counter ions surrounding a charged particle and the bulk solution.[81] The sign and magnitude of the zeta potential reflect the charge distribution on the surface of metal oxides which is a function of $[H^+]$ and $[OH^-]$.[82] Thus, the pH at the zero point of charge (ZPC), or isoelectric point, is a measure of the acidity or basicity of a material. In general, a low ZPC (i.e. low pH) indicates that the metal oxide surface has low affinity for protons and is therefore acidic. In contrast, a higher ZPC represents a more basic surface. The zeta titration curves for the materials are shown in Fig. 5. The ZPC for CeO_2 was around pH = 7 and is in general agreement with reported literature values.[83, 84] For both P-containing materials, the ZPC was around pH = 2 suggesting that their surfaces were more acidic than that of unmodified CeO_2. This result is consistent with the presence of P-O-H groups suggested by SS NMR and DRIFTS measurements.

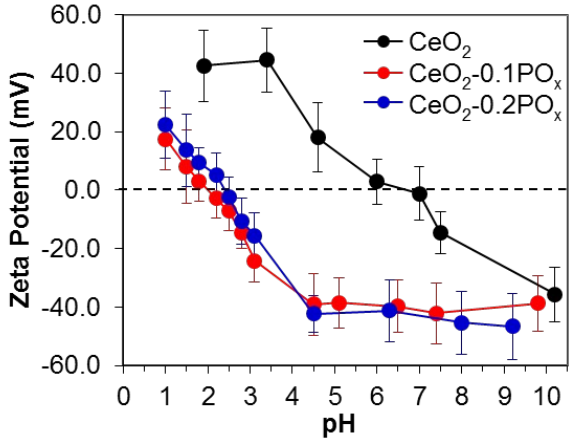

Fig. 5 Zeta titration measurements for the three materials in 0.01 M $KNO_{3(aq)}$. The error bars represent the zeta standard deviation.

View Article Online
DOI: 10.1039/C6TA09703B

The zeta titration measurements indicated that phosphate modification altered the acid-base properties of CeO_2. To further understand these changes, surface acidity was probed via thermal desorption of ammonia (NH_3-TPD). In general, the amount of ammonia desorbed is proportional to the total number of acidic sites while the temperature of desorption is proportional to their acidic strength.[85] The samples were pretreated in O_2-He flow at 500 °C before cooling down to 100 °C for ammonia adsorption. The NH_3-TPD profiles for the two materials are shown in Fig. 6a. CeO_2 showed significant desorption below 200 °C indicating weak interaction with the support possibly through hydrogen bonding with lattice oxygen (i.e. physisorbed). Ammonia desorption continued to about 700 °C with desorption maxima occurring between 200-400 °C and around 600 °C. These results are in agreement with the mild acidity of ceria.[25, 27, 28] The NH_3-TPD integrated value was corrected for multilayer/physisorbed species through profile deconvolution (Fig. S10). After correcting for physisorption, the acid site density for CeO_2 was 2.0 µmol m^{-2}. This value agrees well with prior studies using NH_3 adsorption microcalorimetry (1.9 ± 0.3 µmol m^{-2}).[86-89] The NH_3-TPD profile for the phosphate-modified materials showed significant differences compared to CeO_2. Most notable was a higher amount of desorbed ammonia between 100-300 °C and very little desorption between 300-400 °C. There was also a broad desorption from 400-700 °C. The profile indicated that the surface acidity was altered, in agreement with zeta titration data, and that there seems to be a larger fraction of physisorbed (< 200 °C) or weak acidic sites (200-300 °C) for the P-containing materials. Integration showed that the amount of acidic sites was relatively constant among the three materials (0.44, 0.41, 0.44 mmol g^{-1} for CeO_2, CeO_2-0.1PO_x, and CeO_2-0.2PO_x, respectively).

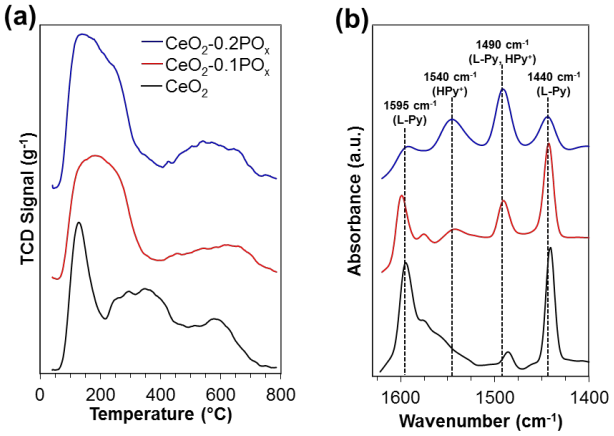

Fig. 6 (a) NH_3-TPD profiles, and (b) DRIFT spectra for the three materials after adsorption of pyridine. The legend is the same as in (a) and all the profiles are shifted for clarity.

Pyridine adsorption was used to probe the strength and type (Lewis vs. Brønsted) of acidic sites by monitoring with IR spectroscopy. Coordination of pyridine molecule to a Lewis acid (L-Py) results in IR bands around 1590-1630 cm^{-1} and 1440 cm^{-1}, attributable to the v8a and v19b pyridine vibrational modes, respectively.[90, 91] Pyridine interaction with Brønsted acidic sites (HPy^+) results in formation of the pyridinium cation and its characteristic v19b vibrational mode at 1540-1545 cm^{-1}.[90, 91] For pyridine adsorbed on CeO_2 (Fig. 6b), the v8a and v19b bands were found at 1595 cm^{-1} and 1440 cm^{-1}, respectively, and were attributed to coordination to Lewis acid sites (i.e. Ce cation). There was a shoulder band around 1575 cm^{-1} and it was assigned to the v8b mode of pyridine bound to cerium cation.[90] The shoulder slowly decreased in intensity to baseline value and could be caused by perturbation by adsorbed carbonates.[26] The band at 1487 cm^{-1} arose due to the v19a vibrational mode of Lewis-bound pyridine and pyridinium cation.[91] Since there was no significant pyridinium band at 1540 cm^{-1}, the 1487 cm^{-1} band was attributed to cerium-coordinated pyridine. These results indicated that CeO_2 contains only weak Lewis acids and is in agreement with previous studies.[25-28]

Similar spectral features were observed for pyridine adsorbed on CeO_2-0.1PO_x. The v8a and v19b bands for cerium-coordinated pyridine were found at 1599 cm^{-1} and 1443 cm^{-1}, respectively. The similar absorption band frequency for Lewis acid-coordinated pyridine (v8a) on CeO_2 and CeO_2-0.1PO_x materials suggested most of the adsorbed pyridine was interacting with cerium cations and that the Lewis acid strength was basically unchanged.[90-93] There was also a small band at 1542 cm^{-1} attributable to the v19b vibrational mode of the pyridinium cation, suggesting the presence of Brønsted acidic sites not observed in CeO_2. Formation of Brønsted sites was also confirmed on CeO_2-0.2PO_x, for which the pyridinium band was clearly observed at 1540 cm^{-1}. It is worth noting that the band integral at 1440 cm^{-1} decreased as the phosphorus loading increased. This suggests formation of Brønsted sites at the expense of Lewis acidic sites.

Table 2 Brønsted and Lewis acidic site distribution and quantification.

Material	Brønsted Acid (mmol g^{-1})[a]	Lewis Acid (mmol g^{-1})[b]	P_{surf}/Ce_{surf}[c]
CeO_2	0	0.44	0
CeO_2-0.1PO_x	0.18 ± 0.01	0.23	0.44
CeO_2-0.2PO_x	0.31 ± 0.04	0.13	0.73

[a]Calculated from cationic exchange with ammonium acetate. [b]Obtained from NH_3-TPD integration after subtracting Brønsted acid sites and correcting for physisorption (see Fig. S10). [c]Calculated assuming that all P-species reside on the surface and a cerium surface density of 7.9 Ce-atom nm^{-2}.[66]

The Brønsted acidic sites were quantified through cation exchange with an aqueous ammonium acetate (pH = 6.99) solution.[94] The number of acidic protons displaced by ammonium cations (24 h exchange) was determined by pH measurement of the resulting suspension (Table 2). To this effect, a calibration curve was prepared based on the pH of an aqueous ammonium acetate solution after addition of known amounts of standardized acetic acid solution. For CeO_2, the pH of the suspension was higher than the ammonium acetate solution, which is consistent with the mild basicity of ceria. In

View Article Online
DOI: 10.1039/C6TA08703F

agreement with the zeta potential measurements, this result suggests there were no exchangeable protons for CeO_2 at pH = 7. The result is also consistent with the pyridine adsorption experiments, and indicated that cerium cations did not have sufficient Lewis acidity to dissociate water, which would result in a decreased pH value. Therefore, any observed decrease in the pH of the phosphated ceria suspensions could be solely attributed to cationic exchange of H^+ for NH_4^+. For CeO_2-0.1PO_x and CeO_2-0.2PO_x the concentrations of Brønsted acidic sites were 0.18 and 0.31 mmol g^{-1}, respectively. The relative increase of exchangeable H^+ between CeO_2-0.1PO_x and CeO_2-0.2PO_x was identical to the relative increase of P-loading (0.7) and suggests that the number of Brønsted acid sites was directly proportional to the phosphorous loading. The cationic exchange experiments also indicated that the ratio between Brønsted acidic protons and P-loading was about 0.3 for both materials. The number of Lewis acidic sites for the materials was estimated by subtracting the quantities of physisorbed ammonia (Fig. S10) and Brønsted acid sites from the NH_3-TPD integrated value. The number of Lewis acidic sites decreased as the number of Brønsted acid sites increased with increasing P content (Table 2). These results are consistent with the changes in relative intensities of HPy^+ and L-Py bands observed in the pyridine adsorption experiments. Furthermore, the fraction of Brønsted sites determined from cationic exchange relative to the total acidic sites from NH_3-TPD agrees well with the theoretical phosphorous surface coverage (Table 2). This suggests that most phosphates were confined to the surface of ceria.

Table 3 Deuterolysis of propylene oxide.[a]

Catalyst	Time (h)	Conversion (%)	PG Yield (%)	TOF[b] (h^{-1})
CeO_2	3	12	12	5.8
CeO_2-0.1PO_x	1	32	32	44
CeO_2-0.2PO_x	1	74	74	100

[a]Conditions: ~10 mg of catalyst, T = 60 °C, D_2O (1 mL), propylene oxide = 0.6 mmol. [b]TOF defined as moles of converted substrate per mole of total acidic sites per reaction time.

The catalytic activity of the three materials was assessed through the deuterolysis of propylene oxide to yield propylene glycol-d2. Deuterolysis/hydrolysis can be catalyzed by acids and bases, but it has been shown that the active site for deuterolysis/hydrolysis using ceria is the water-tolerant Lewis-acidic cerium cation.[95] The catalytic results are summarized in Table 3. For CeO_2, the propylene glycol-d2 yield was 12 % after 3 h reaction time. This corresponds to a turnover frequency (TOF) of 5.8 h^{-1} calculated using the total concentration of acid sites (Brønsted and Lewis) from Table 2. Deuterolysis carried out using CeO_2-0.1PO_x resulted in a TOF of 44 h^{-1}, while the TOF for CeO_2-0.2PO_x increased to 100 h^{-1}. The results indicate that the difference in activity between the three materials can be attributed to the presence and amount of Brønsted acidic sites. ICP analysis of the supernatant from the reaction catalyzed by CeO_2-0.2PO_x showed only traces of P (less than 0.2% of the original P), indicating that the catalyst was stable to the reaction conditions. Recycling experiments also supported these results (Fig. S11).

Previous oxygen isotopic exchange studies have indicated that the amount of labile surface and bulk oxygen in ceria are significantly reduced upon contamination with phosphorous.[59-61] This leads to suppression of redox activity over ceria catalysts (e.g. CO oxidation). It was suggested that the suppression could be caused by surface phosphates blocking coordinatively unsaturated cerium sites (*cus*-Ce) and/or P(V) atoms inhibiting the diffusion of oxygen species within the subsurface region due to lower oxygen vacancy concentrations.[60, 61] In this study, the influence of phosphate loading on the redox properties of the materials was probed through the photocatalytic decomposition of indigo carmine. When ceria is irradiated, electrons from the O_{2p} valence band are excited to the Ce_{4f} conduction band to form electron-hole pairs (i.e. redox pairs).[96] Oxygen vacancies can act as electron capture centers and inhibit electron-hole recombination events thereby improving photocatalytic activity.[97-102] Thus, the photocatalytic activity of ceria is directly related to defect concentration, which in turn is known to correlate to the ease and occurrence of Ce^{3+}/Ce^{4+} redox cycling.[8, 103] The indigo carmine photodegradation activity over the three supports is shown in Table 4. There was almost no redox activity over CeO_2-0.2PO_x as it gave similar conversion to the blank (i.e. no catalyst), while CeO_2-0.1PO_x and CeO_2 were redox active. Clearly, an inverse relationship exists between phosphate loading and photocatalytic activity (i.e. redox ability). In addition, there was a direct relationship between redox activity and the number of *cus*-Ce (i.e. Lewis acidity). This suggests that *cus*-Ce and redox activity are directly related to one another. This is consistent with many redox processes over ceria-based materials that require substrate binding or activation through coordination to cerium cations.[104] The results shown here demonstrate that ceria can be functionalized with Brønsted acids while maintaining its redox properties.

Table 4 Photodegradation of indigo carmine.[a]

Catalyst	Time (h)	Conversion (%)
Blank	1.5	1.8
CeO_2	1.5	58
CeO_2-0.1PO_x	1.5	28
CeO_2-0.2PO_x	1.5	4.1

[a]Conditions: 18.3 ppm indigo carmine (λ_{max} = 610 nm), 2.0 mL water, 4.1 mg of catalyst, irradiation λ = 350 nm.

The introduction of Brønsted acidic sites to ceria while maintaining redox activity could lead to catalysts useful for biomass upgrading technology. An important target in biomass

View Article Online
DOI: 10.1039/C6TA08703E

processing is the selective deconstruction of lignin via reductive cleavage of C-O bonds (i.e. hydrogenolysis),[105] which can be achieved by the combined action of redox and acidic catalysts. Lee *et al.* studied the role of noble metal and acidic alumina-based supports in the hydrodeoxygenation of the lignin model guaiacol to cyclohexane.[106] Their data indicated that noble metals catalyzed the hydrogenation of the aromatic ring while the presence and quantity of acidic sites on the support had a positive effect on the deoxygenation activity. Ceria-based materials are also active for hydrogenolysis of bio-derived compounds even though ceria is considered a mildly basic oxide. The activity has been attributed to the redox capacity of the catalyst components. For example, Schimming *et al.* studied the hydrogenolysis of guaiacol to phenol over ceria-zirconia catalysts and observed a direct correlation between hydrogenolysis activity and catalyst redox properties.[107] Ring saturation products were not observed due to the absence of metals that are active for aromatic hydrogenation. Furthermore, Ota *et al.* studied the hydrogenolysis of vicinal OH groups over a rhenium catalyst promoted by palladium and ceria support.[108] The rhenium component was active for the hydrogenolysis reaction mediated through a Re redox cycle whereas the palladium and ceria components were active for hydrogenation of the alkene intermediate. The results from these studies indicate that both acid and redox sites promote hydrogenolysis activity, while noble metals are needed to provide saturated products.

To this end, catalysts were prepared by deposition of Pd onto the three supports. EDS elemental mapping of Pd/CeO_2-$0.1PO_x$ acquired on STEM images suggests Pd and P species are homogeneously dispersed on the surface of the material (Fig. 7), which is consistent with PXRD patterns and chemisorption measurements (Table S1, Fig. S12).

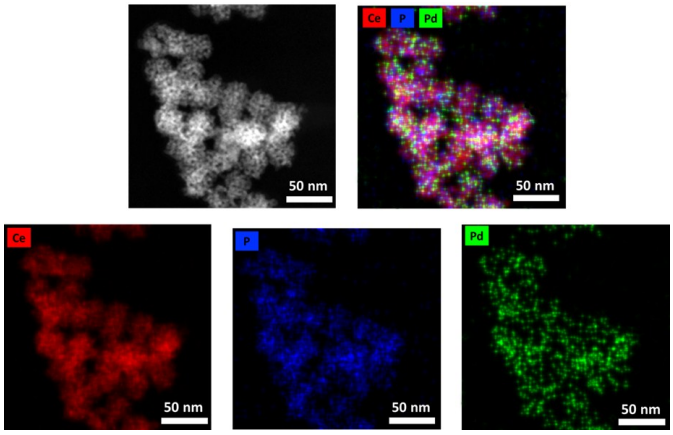

Fig. 7 STEM image and corresponding EDS elemental maps for Pd/CeO_2-$0.1PO_x$.

Reactivity trends and hydrogenolysis activity towards a lignin model compound (eugenol) were assessed by monitoring product yields (Scheme 2). The role of Pd is to provide active hydrogen through molecular dissociation and is considered to be uniform over all three catalysts. That is, no trend exists between yields and Pd dispersion, suggesting hydrogen dissociation is not rate limiting. Pd/CeO_2 was most selective for the fully hydrogenated product (4-propyl-2-methoxycylcohexanol, 59 % yield) (Fig. S13, Table S2). The result is consistent with previous studies that demonstrated phenolics can be activated towards dearomatization over ceria-based catalysts by forming cerium-coordinated phenoxy species.[62] Since Pd/CeO_2 contained the most *cus*-Ce (Table 2), this catalyst should have the largest concentration of activated phenoxy species, which explains the high yield of dearomatized product. In contrast to Pd/CeO_2, Pd/CeO_2-$0.2PO_x$ showed a lower dearomatization yield (27 %) and a higher yield for the allyl hydrogenation product (4-propyl-2-methoxyphenol, 37 %) (Fig. S13, Table S2). The lower yield of dearomatization product is likely due to the low concentration of *cus*-Ce sites in the Pd/CeO_2-$0.2PO_x$ catalyst (Table 2). With this catalyst, phosphate binding limited the availability of *cus*-Ce sites, which decreased the number of phenolic molecules that could be activated for dearomatization shifting the selectivity to the allyl hydrogenation product. Pd/CeO_2-$0.1PO_x$ showed intermediate dearomatization yields (36 %) between Pd/CeO_2 and Pd/CeO_2-$0.2PO_x$. (Fig. S13, Table S2). The intermediate yield correlated well with the intermediate amount of *cus*-Ce (Table 2). Both phosphate-modified catalysts (Pd/CeO_2-PO_x) showed increased hydrogenolysis activity relative to palladium supported on unmodified ceria (Pd/CeO_2) (Fig. 8b, Table S2). The hydrogenolysis activity of Pd/CeO_2 (25 % yield of 4-propylcyclohexanol) likely arises from redox active sites (*cus*-Ce and/or Pd) since the support does not contain Brønsted acid sites. The hydrogenolysis activity of Pd/CeO_2-$0.1PO_x$ catalyst was higher than that of Pd/CeO_2-$0.2PO_x$ (55 % versus 36 % yields, respectively) even though the CeO_2-$0.2PO_x$ support had more Brønsted acidic sites, which should promote C-O cleavage. The Pd/CeO_2-$0.1PO_x$ catalyst appears to be the most active for hydrogenolysis of eugenol due to its optimized bifunctionality (*cus*-Ce/redox and Brønsted acidity) (Fig. 8a). That is, the dissociation of phenolics on ceria to form adsorbed phenoxy species requires *cus*-Ce (or Lewis acid) sites that are active for phenolic dearomatization. The dearomatized product is more prone to acid-catalyzed methoxy cleavage than the aromatic methoxy due to the weaker C-O bonds of the former.[47, 109-112] Thus, the *cus*-Ce sites appear to be necessary for efficient eugenol dearomatization, whereas the redox active *cus*-Ce sites and Brønsted acid group facilitate methoxy removal of the saturated intermediate. The acid and redox site cooperativity was also evident during guaiacol hydrotreatment (Fig. S14, Table S3).

Scheme 2 Products from eugenol hydrotreatment.

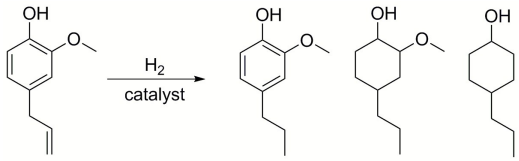

View Article Online
DOI: 10.1039/C6TA08703E

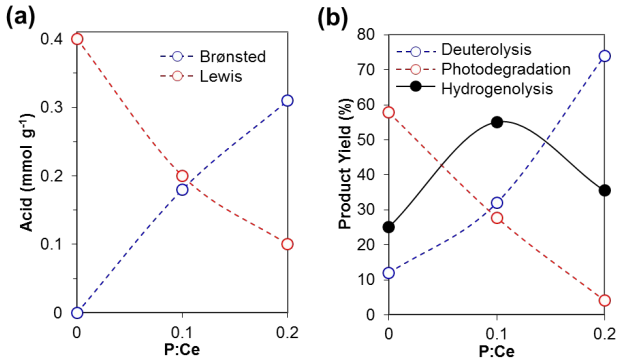

Fig. 8 (a) Brønsted and Lewis acid surface concentrations as a function of P:Ce. (b) Product yields for deuterolysis of propylene oxide, photodegradation of indigo carmine, and hydrogenolysis of eugenol as a function of P:Ce. Conditions for deuterolysis and photodegradation are found in Tables 3 and 4. Conditions for eugenol hydrogenolysis: T = 100 °C, t = 4 h, P_{H2} = 10 bar, Pd : Eugenol = 5 mol. %, 25 mL H_2O.

Conclusions

Deposition of trimethylphosphate onto ceria followed by thermal treatment leads to the formation of surface phosphates while retaining the cubic fluorite structure of ceria. The phosphates introduce Brønsted acidity to the ceria surface at the expense of Lewis acidic sites. The relative amounts of the two types of acidic sites can be controlled by varying the amount of trimethylphosphate deposited onto the ceria. This work demonstrates that ceria can be functionalized with Brønsted acids while still exhibiting redox activity. Furthermore, the redox-to-Brønsted acid ratios can be tuned to achieve the desired activity and selectivity, as demonstrated by the eugenol hydrogenolysis activity. The decomposition of trimethylphosphate to form Brønsted acidic surface phosphates is an important first step in developing redox active ceria-based materials with tailorable functionalities. Further studies exploring derivatized organophosphates and phosphonates will likely uncover new possibilities for introducing other functionalities to the surface of ceria.[113]

Acknowledgements

This research is supported by the U.S. Department of Energy, Office of Science, Basic Energy Sciences, Division of Chemical Sciences, Geosciences, and Biosciences, through the Ames Laboratory Catalysis Science program. Application of the findings to lignin models was performed within the Laboratory Directed Research and Development Program (LDRD) of the Ames Laboratory. The Ames Laboratory is operated for the U.S. Department of Energy by Iowa State University under Contract No. DE-AC02-07CH11358.

References

1 A. Trovarelli, *Catalysis by Ceria and Related Materials*, Imperial College Press, London, 2002.
2 A. Trovarelli, *Catal. Rev.*, 1996, **38**, 439-520.
3 A. Trovarelli, C. de Leitenburg, M. Boaro and G. Dolcetti, *Catal. Today*, 1999, **50**, 353-367.
4 T. Montini, M. Melchionna, M. Monai and P. Fornasiero, *Chem. Rev.*, 2016, **116**, 5987–6041.
5 C. T. Campbell and C. H. Peden, *Science*, 2005, **309**, 713-714.
6 F. Esch, S. Fabris, L. Zhou, T. Montini, C. Africh, P. Fornasiero, G. Comelli and R. Rosei, *Science*, 2005, **309**, 752-755.
7 Y. Lin, Z. Wu, J. Wen, K. R. Poeppelmeier and L. D. Marks, *Nano Lett*, 2014, **14**, 191-196.
8 E. Mamontov, T. Egami, R. Brezny, M. Koranne and S. Tyagi, *J. Phys. Chem. B*, 2000, **104**, 11110-11116.
9 M. Cargnello, V. V. T. Doan-Nguyen, T. R. Gordon, R. E. Diaz, E. A. Stach, R. J. Gorte, P. Fornasiero and C. B. Murray, *Science*, 2013, **341**, 771-773.
10 M. Nolan, *J. Mater. Chem.*, 2011, **21**, 9160-9168.
11 J. Paier, C. Penschke and J. Sauer, *Chem. Rev.*, 2013, **113**, 3949-3985.
12 M. Nolan, S. C. Parker and G. W. Watson, *Surf. Sci.*, 2005, **595**, 223-232.
13 Z. Wu, M. Li, J. Howe, H. M. Meyer and S. H. Overbury, *Langmuir*, 2010, **26**, 16595-16606.
14 N. C. Nelson, B. W. Boote, A. J. Rossini, E. A. Smith and I. I. Slowing, *Submitted*, 2016.
15 H.-X. Mai, L.-D. Sun, Y.-W. Zhang, R. Si, W. Feng, H.-P. Zhang, H.-C. Liu and C.-H. Yan, *J. Phys. Chem. B*, 2005, **109**, 24380-24385.
16 D. Wang, Y. Kang, V. Doan-Nguyen, J. Chen, R. Küngas, N. L. Wieder, K. Bakhmutsky, R. J. Gorte and C. B. Murray, *Angew. Chem. Int. Ed.*, 2011, **50**, 4378-4381.
17 S. Yang and L. Gao, *J. Am. Chem. Soc.*, 2006, **128**, 9330-9331.
18 S. Agarwal, L. Lefferts, B. L. Mojet, D. A. Ligthart, E. J. Hensen, D. R. Mitchell, W. J. Erasmus, B. G. Anderson, E. J. Olivier, J. H. Neethling and A. K. Datye, *ChemSusChem*, 2013, **6**, 1898-1906.
19 Y. Zhang, F. Hou and Y. Tan, *Chem. Commun.*, 2012, **48**, 2391-2393.
20 H.-Z. Zhu, Y.-M. Lu, F.-J. Fan and S.-H. Yu, *Nanoscale*, 2013, **5**, 7219-7223.
21 S. Wang, L. Zhao, W. Wang, Y. Zhao, G. Zhang, X. Ma and J. Gong, *Nanoscale*, 2013, **5**, 5582-5588.
22 J. Lv, Y. Shen, L. Peng, X. Guo and W. Ding, *Chem. Commun.*, 2010, **46**, 5909-5911.
23 M. Tamura, R. Kishi, Y. Nakagawa and K. Tomishige, *Nature Commun.*, 2015, **6**, 8580.
24 D. Singappuli-Arachchige, J. S. Manzano, L. M. Sherman and I. I. Slowing, *ChemPhysChem*, 2016, **17**, 2982-2986.
25 M. I. Zaki, G. A. M. Hussein, S. A. A. Mansour and H. A. El-Ammawy, *J. Molec. Catal.*, 1989, **51**, 209-220.
26 Z. Wu, A. K. P. Mann, M. Li and S. H. Overbury, *J. Phys. Chem. C*, 2015, **119**, 7340-7350.
27 M. Tamura, K.-i. Shimizu and A. Satsuma, *Appl. Catal. A*, 2012, **433–434**, 135-145.

28 C. Binet, M. Daturi and J.-C. Lavalley, *Catal. Today*, 1999, **50**, 207-225.
29 Y. Peng, J. Li, L. Chen, J. Chen, J. Han, H. Zhang and W. Han, *Environ. Sci. Technol.*, 2012, **46**, 2864-2869.
30 Z. Ma, D. Weng, X. Wu and Z. Si, *J. Environ. Sci.*, 2012, **24**, 1305-1316.
31 M. M. Natile, F. Tomaello and A. Glisenti, *Chem. Mater.*, 2006, **18**, 3270-3280.
32 Y. Li, Z. Wei, J. Sun, F. Gao, C. H. F. Peden and Y. Wang, *J. Phys. Chem. C*, 2013, **117**, 5722-5729.
33 Y. Li, H. Cheng, D. Li, Y. Qin, Y. Xie and S. Wang, *Chem. Commun.*, 2008, DOI: 10.1039/B717873E, 1470-1472.
34 W. Shan, F. Liu, H. He, X. Shi and C. Zhang, *Chem. Commun.*, 2011, **47**, 8046-8048.
35 L. Chen, D. Weng, Z. Si and X. Wu, *Progr. Nat. Sci.: Mater. Int.*, 2012, **22**, 265-272.
36 B. Azambre, L. Zenboury, J. V. Weber and P. Burg, *Appl. Surf. Sci.*, 2010, **256**, 4570-4581.
37 S. Gao, X. Chen, H. Wang, J. Mo, Z. Wu, Y. Liu and X. Weng, *J. Colloid Interface Sci.*, 2013, **394**, 515-521.
38 B. M. Reddy, P. M. Sreekanth, P. Lakshmanan and A. Khan, *J. Molec. Catal. A*, 2006, **244**, 1-7.
39 J. Goura and V. Chandrasekhar, *Chem. Rev.*, 2015, **115**, 6854-6965.
40 J. E. Chambers and P. E. Levi, *Organophosphates Chemistry, Fate, and Effects: Chemistry, Fate, and Effects*, Elsevier Science, 2013.
41 K. T. Wong, B. Shong, W. Sun and S. F. Bent, *J. Phys. Chem. C*, 2013, **117**, 26628-26635.
42 M. Timpel, M. V. Nardi, S. Krause, G. Ligorio, C. Christodoulou, L. Pasquali, A. Giglia, J. Frisch, B. Wegner, P. Moras and N. Koch, *Chem. Mater.*, 2014, **26**, 5042-5050.
43 S. H. Pang, C. A. Schoenbaum, D. K. Schwartz and J. W. Medlin, *Nature Commun.*, 2013, **4**.
44 C. A. Schoenbaum, D. K. Schwartz and J. W. Medlin, *Acc. Chem. Res.*, 2014, **47**, 1438-1445.
45 K. Kandel, C. Frederickson, E. A. Smith, Y.-J. Lee and I. I. Slowing, *ACS Catal.*, 2013, **3**, 2750-2758.
46 N. Yan, Y. Yuan, R. Dykeman, Y. Kou and P. J. Dyson, *Angew. Chem. Int. Ed.*, 2010, **49**, 5549-5553.
47 C. Zhao, J. He, A. A. Lemonidou, X. Li and J. A. Lercher, *J. Catal.*, 2011, **280**, 8-16.
48 M. Shetty, K. Murugappan, T. Prasomsri, W. H. Green and Y. Román-Leshkov, *J. Catal.*, 2015, **331**, 86-97.
49 T. J. Thibodeau, A. S. Canney, W. J. DeSisto, M. C. Wheeler, F. G. Amar and B. G. Frederick, *Appl. Catal. A*, 2010, **388**, 86-95.
50 D. R. Moberg, T. J. Thibodeau, F. G. Amar and B. G. Frederick, *J. Phys. Chem. C*, 2010, **114**, 13782-13795.
51 K. Kandel, J. W. Anderegg, N. C. Nelson, U. Chaudhary and I. I. Slowing, *J. Catal.*, 2014, **314**, 142-148.
52 D. A. Chen, J. S. Ratliff, X. Hu, W. O. Gordon, S. D. Senanayake and D. R. Mullins, *Surf. Sci.*, 2010, **604**, 574-587.
53 P. Mäkie, P. Persson and L. Österlund, *J. Phys. Chem. C*, 2012, **116**, 14917-14929.
54 P. Mäkie, G. Westin, P. Persson and L. Österlund, *J. Phys. Chem. A*, 2011, **115**, 8948-8959.
55 M. A. Henderson, *J. Phys. Chem. C*, 2011, **115**, 23527-23534.
56 S. T. Lin and K. J. Klabunde, *Langmuir*, 1985, **1**, 600-605.
57 V. Štengl, J. Henych, T. Grygar and R. Pérez, *Mater. Res. Bull.*, 2015, **61**, 259-269.
58 M. B. Mitchell, V. N. Sheinker, W. W. Cox, E. N. Gatimu and A. B. Tesfamichael, *J. Phys. Chem. B*, 2004, **108**, 1634-1645.
59 L. Xu, G. Guo, D. Uy, A. E. O'Neill, W. H. Weber, M. J. Rokosz and R. W. McCabe, *Appl. Catal. B*, 2004, **50**, 113-125.
60 C. Larese, F. Cabello Galisteo, M. Lopez Granados, R. Mariscal, J. L. G. Fierro, P. S. Lambrou and A. M. Efstathiou, *J. Catal.*, 2004, **226**, 443-456.
61 M. Lopez Granados, F. Cabello Galisteo, P. S. Lambrou, R. Mariscal, J. Sanz, I. Sobrados, J. L. G. Fierro and A. M. Efstathiou, *J. Catal.*, 2006, **239**, 410-421.
62 N. C. Nelson, J. S. Manzano, A. D. Sadow, S. H. Overbury and I. I. Slowing, *ACS Catal.*, 2015, **5**, 2051-2061.
63 C. Hardacre, G. M. Roe and R. M. Lambert, *Surf. Sci.*, 1995, **326**, 1-10.
64 M. Romeo, K. Bak, J. El Fallah, F. Le Normand and L. Hilaire, *Surf. Interface Anal.*, 1993, **20**, 508-512.
65 M. Feike, D. E. Demco, R. Graf, J. Gottwald, S. Hafner and H. W. Spiess, *J. Magn. Reson., Series A*, 1996, **122**, 214-221.
66 Y. Madier, C. Descorme, A. M. Le Govic and D. Duprez, *J. Phys. Chem. B*, 1999, **103**, 10999-11006.
67 F. A. Miller and C. H. Wilkins, *Anal. Chem.*, 1952, **24**, 1253-1294.
68 T. Masui, H. Hirai, N. Imanaka and G. Adachi, *Physica Status Solidi (a)*, 2003, **198**, 364-368.
69 A. Hezel and S. D. Ross, *Spectrochimica Acta*, 1966, **22**, 1949-1961.
70 S. E. Stein, "Infrared Spectra", National Institute of Standards and Technology, Gaithersburg MD, 20899, http://webbook.nist.gov, (accessed June 29, 2016, 2016).
71 A. Pfau and K. D. Schierbaum, *Surf. Sci.*, 1994, **321**, 71-80.
72 M. A. Henderson, C. L. Perkins, M. H. Engelhard, S. Thevuthasan and C. H. F. Peden, *Surf. Sci.*, 2003, **526**, 1-18.
73 D. R. Mullins, S. H. Overbury and D. R. Huntley, *Surf. Sci.*, 1998, **409**, 307-319.
74 S. M. F. Shahed, T. Hasegawa, Y. Sainoo, Y. Watanabe, N. Isomura, A. Beniya, H. Hirata and T. Komeda, *Surf. Sci.*, 2014, **628**, 30-35.
75 J. W. Wiench, M. Pruski, B. Tischendorf, J. U. Otaigbe and B. C. Sales, *J. Non-Cryst. Sol.*, 2000, **263–264**, 101-110.
76 L. Karpowich, S. Wilcke, R. Yu, G. Harley, J. A. Reimer and L. C. De Jonghe, *J. Solid State Chem.*, 2007, **180**, 840-846.
77 X. Xue and M. Kanzaki, *J. Am. Ceram. Soc.*, 2009, **92**, 2803-2830.
78 A. K. Cheetham, N. J. Clayden, C. M. Dobson and R. J. B. Jakeman, *J. Chem. Soc., Chem. Commun.*, 1986, 195-197.
79 M. Bak, J. T. Rasmussen and N. C. Nielsen, *J. Magn. Reson.*, 2000, **147**, 296-330.
80 A. Bax, R. H. Griffey and B. L. Hawkins, *J. Magn. Reson.*, 1983, **55**, 301-315.

81 R. J. Hunter, in *Zeta Potential in Colloid Science*, Academic Press, New York, 1981, ch. 1, pp. 1-10.
82 G. A. Parks, *Chem. Rev.*, 1965, **65**, 177-198.
83 P. Suphantharida and K. Osseo-Asare, *J. Electrochem. Soc.*, 2004, **151**, G658-G662.
84 M. Kosmulski, *Chemical Properties of Material Surfaces*, CRC Press, 2001.
85 Determination of Acidic and Basic Properties on Solid Surfaces. in *Studies in Surface Science and Catalysis*, eds. K. Tanabe, M. Misono, Y. Ono and H. Hattori, Elsevier, Tokyo, 1989, Vol. 51, pp. 5-25.
86 D. Stošić, S. Bennici, V. Rakić and A. Auroux, *Catal. Today*, 2012, **192**, 160-168.
87 M. G. Cutrufello, I. Ferino, R. Monaci, E. Rombi and V. Solinas, *Top. Catal.*, 2002, **19**, 225-240.
88 B. Bonnetot, V. Rakic, T. Yuzhakova, C. Guimon and A. Auroux, *Chem. Mater.*, 2008, **20**, 1585-1596.
89 X. Ge, S. Hu, Q. Sun and J. Shen, *J. Nat. Gas Chem.*, 2003, **12**, 119-122.
90 C. H. Kline and J. Turkevich, *J. Chem. Phys.*, 1944, **12**, 300-309.
91 E. P. Parry, *J. Catal.*, 1963, **2**, 371-379.
92 C. Morterra and G. Magnacca, *Catal. Today*, 1996, **27**, 497-532.
93 J. A. Lercher, C. Gründling and G. Eder-Mirth, *Catal. Today*, 1996, **27**, 353-376.
94 V. C. F. Holm, G. C. Bailey and A. Clark, *J. Phys. Chem.*, 1959, **63**, 129-133.
95 Y. Wang, F. Wang, Q. Song, Q. Xin, S. Xu and J. Xu, *J. Am. Chem. Soc.*, 2013, **135**, 1506-1515.
96 P. Patsalas, S. Logothetidis, L. Sygellou and S. Kennou, *Phys. Rev. B*, 2003, **68**, 035104.
97 A. D. Liyanage, S. D. Perera, K. Tan, Y. Chabal and K. J. Balkus, *ACS Catal.*, 2014, **4**, 577-584.
98 J. Wang, P. Liu, X. Fu, Z. Li, W. Han and X. Wang, *Langmuir*, 2009, **25**, 1218-1223.
99 Z. Zhang, W. Wang, E. Gao, M. Shang and J. Xu, *J. Haz. Mater.*, 2011, **196**, 255-262.
100 T. Tachikawa and T. Majima, *J. Am. Chem. Soc.*, 2009, **131**, 8485-8495.
101 M. a. D. Hernández-Alonso, A. B. Hungría, A. Martínez-Arias, M. Fernández-García, J. M. Coronado, J. C. Conesa and J. Soria, *Appl. Catal. B*, 2004, **50**, 167-175.
102 Y. Li, Q. Sun, M. Kong, W. Shi, J. Huang, J. Tang and X. Zhao, *J. Phys. Chem. C*, 2011, **115**, 14050-14057.
103 M. Mogensen, N. M. Sammes and G. A. Tompsett, *Solid State Ionics*, 2000, **129**, 63-94.
104 D. R. Mullins, *Surf. Sci. Rep.*, 2015, **70**, 42-85.
105 M. P. Pandey and C. S. Kim, *Chem. Eng. Technol.*, 2011, **34**, 29-41.
106 C. R. Lee, J. S. Yoon, Y.-W. Suh, J.-W. Choi, J.-M. Ha, D. J. Suh and Y.-K. Park, *Catal. Commun.*, 2012, **17**, 54-58.
107 S. M. Schimming, O. D. LaMont, M. König, A. K. Rogers, A. D. D'Amico, M. M. Yung and C. Sievers, *ChemSusChem*, 2015, **8**, 2073-2083.
108 N. Ota, M. Tamura, Y. Nakagawa, K. Okumura and K. Tomishige, *Angew. Chem. Int. Ed.*, 2015, **54**, 1897-1900.
109 S. W. Benson, *Thermochemical Kinetics: Methods for the estimation of thermochemical data and rate parameters*, John Wiley & Sons, Inc., New York, 1976.
110 S. J. Blanksby and G. B. Ellison, *Acc. Chem. Res.*, 2003, **36**, 255-263.
111 P. M. Mortensen, J. D. Grunwaldt, P. A. Jensen, K. G. Knudsen and A. D. Jensen, *Appl. Catal. A*, 2011, **407**, 1-19.
112 P. M. Mortensen, J.-D. Grunwaldt, P. A. Jensen and A. D. Jensen, *ACS Catal.*, 2013, **3**, 1774-1785.
113 J. G. Heck, J. Napp, S. Simonato, J. Möllmer, M. Lange, H. M. Reichardt, R. Staudt, F. Alves and C. Feldmann, *J. Am. Chem. Soc.*, 2015, **137**, 7329-7336.

View Article Online
DOI: 10.1039/C6TA08703E

Table of contents entry:

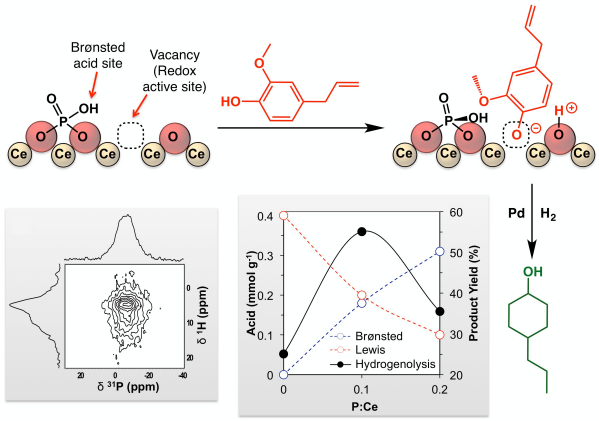

Text for the graphic:

Modification of ceria surface with phosphates leads to acid/redox active materials that can serve as non-innocent supports for Pd-catalyzed hydrogenolysis of lignin model compounds.